DRAFT VERSION APRIL 3, 2024
Preprint typeset using LaTeX style emulateapj v. 5/2/11

STELLAR CORONAE, SOLAR FLARES: A DETAILED COMPARISON OF σ Gem, HR 1099, AND THE SUN IN HIGH-RESOLUTION X-RAYS

DAVID P. HUENEMOERDER[A], KENNETH J. H. PHILLIPS[B], JANUSZ SYLWESTER[C], BARBARA SYLWESTER[C]

Draft version April 3, 2024

ABSTRACT

The *Chandra* High Energy Transmission Grating Spectrometer (HETG) spectra of the coronally active binary stars σ Gem and HR 1099 are among the highest fluence observations for such systems taken at high spectral resolution in x-rays with this instrument. This allows us to compare their properties in detail to solar flare spectra obtained with the Russian *CORONAS-F* spacecraft's RESIK instrument at similar resolution in an overlapping bandpass. Here we emphasize the detailed comparisons of the 3.3–6.1 Å region (including emission from highly ionized S, Si, Ar, and K) from solar flare spectra to the corresponding σ Gem and HR 1099 spectra. We also model the the larger wavelength range of the HETG, from 1.7–25 Å—having emission lines from Fe, Ca, Ar, Si, Al, Mg, Ne, O, and N—to determine coronal temperatures and abundances. σ Gem is a single-lined coronally active long-period binary which has a very hot corona. HR 1099 is a similar, but shorter period, double-lined system. With very deep HETG exposures we can even study emission from some of the weaker species, such as K, Na, and Al, which are important since they have the lowest first ionization potentials, a parameter well known to be correlated with elemental fractionation in the solar corona. The solar flare temperatures reach ≈ 20 MK, comparable to the σ Gem and HR 1099 coronae. During the Chandra exposures, σ Gem was slowly decaying from a flare and its spectrum is well characterized by a collisional ionization equilibrium plasma with a broad temperature distribution ranging from 2–60 MK, peaking near 25 MK, but with substantial emission from 50 MK plasma. We have detected K XVIII and Na XI emission which allow us to set limits on their abundances. HR 1099 was also quite variable in x-rays, also in a flare state, but had no detectable K XVIII. These measurements provide new comparisons of solar and stellar coronal abundances, especially at the lowest FIP values. The low FIP elements do not show enhancement in the stellar coronae as they do in the Sun, except perhaps for K in σ Gem. While σ Gem and HR 1099 differ in their emission measure distributions, they have very similar elemental abundances.

Subject headings: stars: coronae — stars: late-type — stars: individual (σ Gem) — stars: individual (HR 1099) — X-rays: stars

1. INTRODUCTION

Accurate knowledge of elemental abundances is of fundamental importance for many astrophysical processes. In soft x-rays from hot, low-density plasmas ($\lambda \sim$ 1–100 Å, or $E \sim$ 0.1–12 keV; $T \sim$ 1–100 MK; $n_e \lesssim 10^{12}\,\mathrm{cm}^{-3}$) in collisional ionization equilibrium, emission processes are relatively simple in that every collisional excitation results in a radiative transition whose photon escapes the plasma. At coronal temperatures, ions are highly charged and the dominant species are typically H- and He-like ions. The abundant elements from C to Fe have their principal H- and He-like lines in this band. Hence, high-resolution x-ray spectra provide a wealth of emission lines from numerous abundant elements over a range of temperatures from a plasma which is relatively easily modeled.

The solar corona and coronae of other stars still have some unexplained properties related to their elemental abundances, and these, in turn, relate to the formation of coronae and their use as diagnostics of stellar abundances. It has been known for quite some time that there is a correlation of solar coronal abundances with the elements' first ionization potentials (FIP) in the sense that elements with low FIP ($\lesssim$ 10 eV) are enhanced by up to a factor of 4 over photospheric values (Feldman 1992; Feldman & Laming 2000).

In other stars, coronal abundance anomalies were suspected even with low-resolution *ASCA* spectra (Kaastra et al. 1996), but there the low-FIP elements were depleted relative to solar photospheric values (termed an inverse FIP effect). With the advent of high-resolution spectroscopy with the *Chandra* X-ray Observatory (CXO) and *XMM-Newton* grating instruments nearly a decade ago, these results were confirmed in detail (Audard, Güdel & Mewe 2001; Brinkman et al. 2001). The stellar observations have several difficulties in interpretation and in direct comparison to the Sun. The photospheric abundances are often unknown, so the comparison is done against solar values. The stellar disks are unresolved; we do not know whether particular structures, such as actively flaring regions or quiescent loops, dominate the emission, nor how extended are such structures. Since flares in the Sun—and presumably other stars—heat and evaporate chromospheric plasmas, it has been suggested that the flare matter would more likely represent the underlying photospheric plasma, since purported diffusion processes sensitive to the FIP have had no time to have effect. Observational results have been mixed. Nordon & Behar (2008) found no strong or consistent correlation of abundance changes during stellar flares. From low-resolution, few-temperature-component models, Liefke, Fuhrmeister & Schmitt (2010) found a factor of three increase in Fe abundance over the quiescent value during a large flare on CN Leo; they could detect no effect in other elements. Wood & Linsky (2010) and Wood, Laming & Karovska (2012) examined the FIP effect in M-dwarfs and found that both high and low activity stars can have an inverse FIP effect. They suggested that there is a

[a] Massachusetts Institute of Technology, Kavli Institute for Astrophysics and Space Research, 70 Vassar St., Cambridge, MA, 02139, USA (dph@space.mit.edu)
[b] Visiting Scientist, Space Research Center, Polish Academy of Sciences, 51-622, Kopernika 11, Wrocław, Poland (kennethjhphillips@yahoo.com)
[c] Space Research Center, Polish Academy of Sciences, 51-622, Kopernika 11, Wrocław, Poland (js@cbk.pan.wroc.pl, bs@cbk.pan.wroc.pl)

trend with spectral type and that stars of type K are unbiased, earlier types have a FIP effect, and later types have an inverse FIP effect.

Laming & Hwang (2009) and Laming (2012) have presented a theoretical basis for low-FIP ion fractionation in coronal loops via ponderomotive forces associated with Alfvén waves passing through the loops. Some elements can be either enhanced or depleted in the corona relative to the photosphere, depending upon the direction of the ponderomotive force. Calculations of fractionation amounts with model loops having typical parameters are similar to those observed.

The determination of abundances from x-ray spectra can have far-reaching implications. Drake & Testa (2005) used the rather uniform values of the Ne:O abundance ratio in many stars to argue that these elements do not undergo differential fractionation, but represent the cosmic abundance ratio, and so adoption of this ratio for the Sun would reconcile a rather serious conflict with stellar interior models and helioseismology.

Here we present new results for the lowest FIP elements, K and Na, in the *Chandra*/HETG spectra of σ Gem and HR 1099. By modeling the HETGS spectra over the 1–25 Å range, we also derive the emission measure distributions and elemental abundances of all the major contributors, which span a broad range in FIP. These models improve on prior work on these *Chandra* spectra (e.g. Drake et al. 2001; Nordon & Behar 2007, 2008).

To compare σ Gem and HR 1099 to the Sun, we use a high-resolution x-ray spectrum from the *CORONAS-F* RESIK instrument of a solar flare on 2002 December 26, in which the high-temperature plasmas reach the mid-range of temperatures found in the stellar spectra whose emissions are also probably due, in large part, to stellar flares, as we will show for σ Gem here, and as has been shown for HR 1099 by Nordon & Behar (2007).

2. OBSERVATIONS AND CALIBRATION

2.1. *Chandra/HETG*

The *Chandra*/HETG instrument (Canizares et al. 2005) observed σ Gem and HR 1099 twice each; dataset identifiers and exposure times for each star are given in Table 1. The HETGS spectra cover the range from about 1–30 Å, as dispersed by two types of grating facets, the High Energy Grating (HEG) and the Medium Energy Grating (MEG), with resolving powers of between about 100 to 1000, with approximately constant full-width-half-maxima (FWHM) of 12 mÅ for HEG and 23 mÅ for MEG. These two objects have the highest fluence exposures among hot, coronally active stars observed with the HETGS; there are about 350,000 counts for each star in the combined first orders over the 2–15 Å range covered by both MEG and HEG. The only other similar source with more counts is Capella (a calibration object) having 20 HETGS exposures for nearly 800,000 counts. Capella, however, is much cooler than σ Gem and HR 1099 and has relatively little flux in the 3–6 Å region—about 10% that of the other two stars.

The *Chandra* data were reprocessed with standard Chandra Interactive Analysis of Observations (CIAO) programs (Fruscione et al. 2006) to apply the most recent calibration data (CIAO 4.4 and the corresponding calibration database as of 2012 June 19). Since these are very bright sources with saturated and distorted zeroth order images, and since the zeroth order provides the origin for the wavelength scale, we determined the zeroth order centroid from the intersection of a grating spectrum with the strong zeroth order CCD frame-shift streak. The default binning was adopted, which over-samples the instrumental resolution by about a factor of 4. The counts spectra are thus composed of 4 orders per source per observation: the ± 1 orders for each grating type, the MEG and HEG, which have different efficiencies and resolving powers.

Table 1
Stellar/Observational Information

Property	σ Gem	HR 1099
Chandra dataset IDs	5422, 6282	1252, 62538
Date Obs	2005-05-16,17	1999-09-14,17
HETG Exposures [ks]	62.8, 57.9	14.7, 94.7
Spectral Type	K1 III + ?	K1 IV + G5 IV
d[pc]	37.5	30.68
$N_{\rm H}$ [10^{18} cm^{-2}]	1.0	0.94
L_{bol}[10^{34} ergs s^{-1}]	21.4	3.23
L_x[10^{31} ergs s^{-1}]	3.0	1.9
VEM [10^{54} cm^{-3}]	2.4	1.5

Note. — Observation dates are the UT day on which the observation started. Spectral types were taken from the compilation of Eker et al. (2008). The neutral hydrogen column densities are from Sanz-Forcada, Brickhouse & Dupree (2002). Distances are from HIPPARCOS (van Leeuwen 2007). Bolometric luminosities and volume emission measure (VEM) were derived using information in Strassmeier (2009). X-ray luminosities are from the model spectra derived herein over the 1–50 Å (0.2–12 keV) band.

Several calibration files are required for analysis to convolve a model flux spectrum with the instrumental response in order to produce model counts. These are made for each observation and each spectral order by the CIAO programs which use observation-specific data in conjunction with the calibration files to make the effective area files ("Auxiliary Response File", or ARF) and the spectral redistribution and extraction-aperture efficiency files ("Response Matrix File", or RMF) (Davis 2001).

We show a portion of the σ Gem and HR 1099 spectra in Figure 1 (top and middle panels).

2.2. *RESIK*

RESIK (REntgenovsky Spekrometr s Izognutymi Kristalami) was a bent crystal spectrometer on the Russian *CORONAS-F* spacecraft viewing solar active regions and flares, and was operational between 2001 and 2003. The instrument consisted of a pair of Si (crystal plane 111) crystals and a pair of quartz $(10\bar{1}0)$ crystals, with a one-dimensional position-sensitive proportional counter for each crystal pair. The combination of bent crystals and position-sensitive detector enables the entire spectral range to be observed simultaneously within a data-gathering interval. The duration of these intervals varied inversely with the amount of incident x-ray emission, typical values being 2 s for flare peaks and up to five minutes for times late in a flare decay. The wavelength ranges of the four channels for on-axis sources were 3.40–3.80 Å (channel 1), 3.83–4.27 Å (2), 4.35–4.86 Å (3), and 5.00–6.05 Å (4). The lack of a collimator allowed RESIK to observe off-axis flares, extending the wavelength limits in one direction or the other by up to 70 mÅ. The low atomic number of the crystal material ensured a much lower background due to crystal fluorescence (which depends on Z^4) than previous solar crystal spectrometers, enabling the solar continuum to be measured for at least the two shorter-wavelength channels.

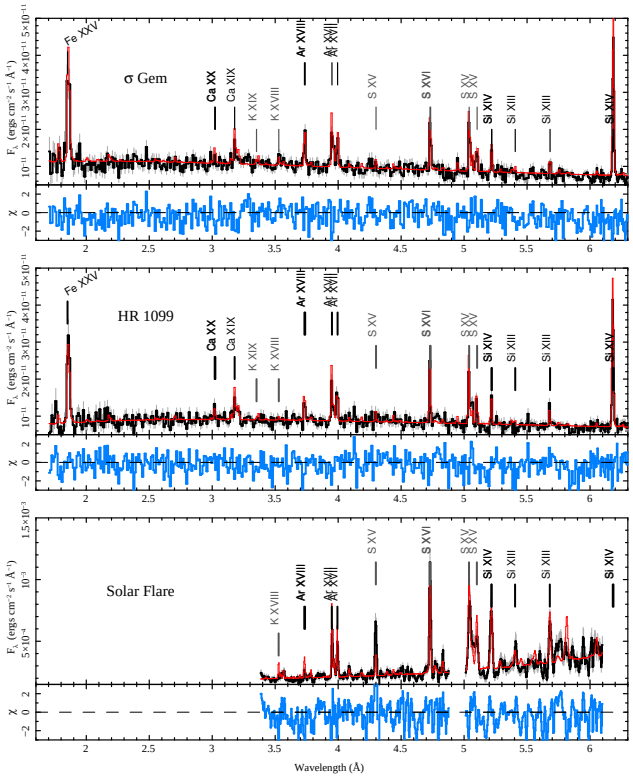

Figure 1. Here we show the spectra and models in the short wavelength region where HETG and RESIK spectra overlap. Flux-corrected spectra are in black, and the red is the model convolved by the instrumental resolution. Below each, in blue, are residuals. The top panel shows σ Gem; the middle is HR 1099; the bottom is the rise phase of solar flare on 2002 December 26 (maximum at 06:30 UT). All models were evaluated using AtomDB emissivities, though the solar spectrum was fit using CHIANTI (Dere et al. 2009). Residuals shown for the solar spectrum include an arbitrary scale factor. Line identifications for prominent or important ions are given. Emission measures and abundances used in the models are given in Figure 3 and Table 2, respectively.

The total wavelength range (3.4–6.05 Å) included resonance lines of He-like K (K XVIII), H-like and He-like Ar (Ar XVIII, Ar XVII), He-like Cl (Cl XVI), H-like and He-like S (S XVI, S XV), and H-like and He-like Si (Si XIV, Si XIII). The wavelength resolution (FWHM) varied from 8 mÅ (near 3.3 Å) to 17 mÅ (near 6 Å). RESIK was unable to resolve thermal Doppler broadening for typical flare temperatures. Thus, for a temperature of 15 MK the thermal Doppler broadening (FWHM) of the K XVIII resonance line at 3.53 Å is 1.6 mÅ, and for the Si XIV line at 5.22 Å it is 2.7 mÅ. Further instrumental details about RESIK are given by Sylwester et al. (2005).

The RESIK spectra thus cover a much more limited wavelength region than the Chandra/HETG spectra but the high quality of the absolute calibration allow a detailed comparison of the abundances of Si, S, Ar, and K in particular.

In the bottom panel of Figure 1 we show a RESIK spectrum taken over a data-gathering interval of 86 s during the rise phase of a GOES class C1.9 flare on 2002 December 26 at 06:30 UT (maximum). Identifications of some of the principal emission lines are given.

3. ANALYSIS

3.1. *HETG Spectral Fitting and Modeling*

The analysis of the HETG spectra required an iterative combination of global plasma model fits, parametric line fitting, and line-based reconstruction of the emission measure distribution (EMD) and elemental abundances. The first step was to fit a plasma model to the binned spectrum in order to provide a physically-based continuum for parametric line fitting. Even at HEG resolution ($FWHM = 12$ mÅ), there are regions of the spectrum for which the apparent continuum is above the true value due to line blending. The continuum originates from free-free (FF) and free-bound (FB) components, and the latter depends significantly upon elemental abundances, especially for solar flares (Phillips et al. 2010); for the stars with high temperatures and low metallicity, FF emission dominates the continuum.

The line emissivities, more generally called $G(T_e)$ functions (in which T_e is the plasma's electron temperature), are defined by the amount of radiation emitted by an optically thin plasma per second with unit volume emission measure ($N_e N_{\rm H} V$ where N_e is the electron density, $N_{\rm H}$ the proton density, and V the emitting volume). In terms of plasma and atomic quantities, we can write $G(T_e)$ for a particular line of element, X, as

$$G(T_e) = \frac{N(X_i^{+n})}{N(X^{+n})} \frac{N(X^{+n})}{N(X)} \frac{N(X)}{N({\rm H})} \frac{A_{i1}}{N_e} \quad [{\rm phot\,cm^3\,s^{-1}}] \quad (1)$$

where $N(X_i^{+n})$ is the population of the excited level-i of an n-times-ionized atom, X_i^{+n}, $N(X^{+n})/N(X)$ is the ion fraction as a function of electron temperature from ionization balance calculations, $N(X)/N({\rm H})$ the abundance of element X relative to hydrogen, and A_{i1} the transition probability from level i to the ground state.

The line luminosity is related to $G(T)$ through an integral over the emission measure, which, through a change of variables, is expressed as a differential in electron temperature instead of volume:

$$L(X_i^{+n}) = \int G(T_e)\,[N_e N_{\rm H} \frac{{\rm d}V}{{\rm d}\log T_e}]\,{\rm d}\log T_e \quad [{\rm phot\,s^{-1}}] \quad (2)$$

(where i and n identify the transition and ion, as in the expression for $G(T_e)$). The quantity in square brackets is called the differential emission measure. When we refer to the emission measure distribution (EMD) it will be this quantity integrated over intervals of $\log T_e$ *vs.* temperature (for historical examples, see Lemen et al. 1989; Jordan 1975; Pottasch 1963).

For the plasma models describing the HETG spectra, we relied on the output of the Astrophysical Plasma Emission Code (APEC), as available in the atomic database, AtomDB (Smith et al. 2001; Foster et al. 2012), which provided continuum and line emissivities for low-density plasmas in collisional ionization equilibrium. We adopted the defaults for ionization balance (Mazzotta et al. 1998) and solar photospheric abundances (Anders & Grevesse 1989) (though abundances were free parameters and referenced to more recent determinations later). The initial fit used a broken power-law model for the emission measure temperature distribution with variable abundances for the most abundant elements with strong emission line features in the HETG spectrum (e.g., N, O, Ne, Mg, Si, S, and Fe). This model allowed a range of temperatures as required for multi-thermal plasmas. Including lines provided strong constraints on dominant temperatures, but the "abundances" were here solely parameters, since the line flux, continuum flux, and abundances are degenerate to

a large degree. The result is a semi-empirical plasma model which follows the observed continuum.

Given a continuum model, we then parametrically fit a large number of lines (in small groups) as a sum of the plasma continuum and Gaussian line profiles. The free parameters were the line wavelengths and fluxes. Since the lines are unresolved (the thermal broadening being below instrumental resolution, and with no detection of other broadening, such as due to turbulence, rotational, or from binary motions), intrinsic widths were typically frozen at a small value (e.g., $2\,\mathrm{m\AA}$). The only exception was for the Ly-α lines of H-like ions which are marginally resolved doublets; and allowing the width to be free was sufficient for an accurate determination of line flux. For regions with heavily blended lines, constraints on line separations were sometimes imposed if the features were well identified (e.g., Ne X Lyman series at ≈ 9.5–12.1 Å blending with the Mg XI triplet at ≈ 9.2 Å). Each line fit had a candidate identification with a transition in AtomDB, based on prior experience with similar spectra (for example, see Huenemoerder et al. 2003; Huenemoerder, Canizares & Schulz 2001), or if it is unknown or an unresolved blend, it may have been fit solely to remove it from an overlapping feature of interest. Lines with large absolute wavelength residuals relative to the AtomDB identification were flagged as probable mis-identifications and excluded from further analysis. We give the line measurements for σ Gem and HR 1099 in Tables 5–6.

The resulting list of lines and fluxes were then used to perform a simultaneous determination of the EMD and elemental abundances. This was done by minimizing the residuals of model and measured fluxes against a smoothness constraint on the EMD, using the emissivities *vs.* temperature taken from AtomDB for each line. The free parameters were the EMD weights in each of 26 logarithmically spaced temperature bins which spanned the sensitivity range of the lines, and the relative abundances. We started with a flat EMD and constant abundances. The constraint was cast in the form of a penalty function proportional to the summed squared second derivative of the EMD, and by fitting the logarithm of the EMD to enforce positivity. Figure 2 shows the temperature regime covered by lines in the HETG bandpass (1.5–25 Å), spanning 1.5–$60\,\mathrm{MK}$. Since the continuum emissivity was not included explicitly in this procedure, the resulting abundance and EMD normalizations are degenerate, requiring a good starting point, and a post facto evaluation of the binned spectrum to evaluate the continuum level. We performed an iteration in which we derived the EMD and abundances, evaluated the model spectrum, scaled the overall EMD normalization and abundances inversely, and repeated the reconstruction until converged. In § A.1, we show the line flux residuals against different parameters to demonstrate the quality of the solutions. Ratios of observed to theoretical fluxes within a factor of 2 are typical of such reconstructions (see, for example Sanz-Forcada, Brickhouse & Dupree 2002).

We tested the EMD/abundance reconstruction method by fitting spectra simulated with sums of 1–3 broken powerlaw EMDs ($EMD \propto (T/T_0)^{\gamma(T)}$). We used different shapes for the input EMD, from single, narrow peaks, to 2–3 peaks of different widths, positions, and weights. The results showed that small wiggles in the EMD (of order 10%) were artifacts, that the EMD peak temperatures could be determined to about 0.1 dex, that abundances could be determined to about 10% accuracy for strong-lined ions (in this self-consistent treatment of the method), and finally that the weak line features should have their abundances fitted post facto using the EMD solution. The simulations also allowed us to tune the smoothness constraint, since if it was too small, much jagged structure appeared in the solution. The top panel of Figure 3 gives a detailed view of the σ Gem and HR 1099 EMDs. Values plotted are the emission measure integrated over 0.1 dex temperature bins. The dip in both curves at just above $10\,\mathrm{MK}$ is probably a reconstruction artifact, as are wiggles on the low-temperature tail. The large peak at about $50\,\mathrm{MK}$ in the σ Gem solution, however, is required by the spectrum (and actually required a slightly more relaxed EMD smoothness constraint than for HR 1099 to give a good match to the model spectrum).

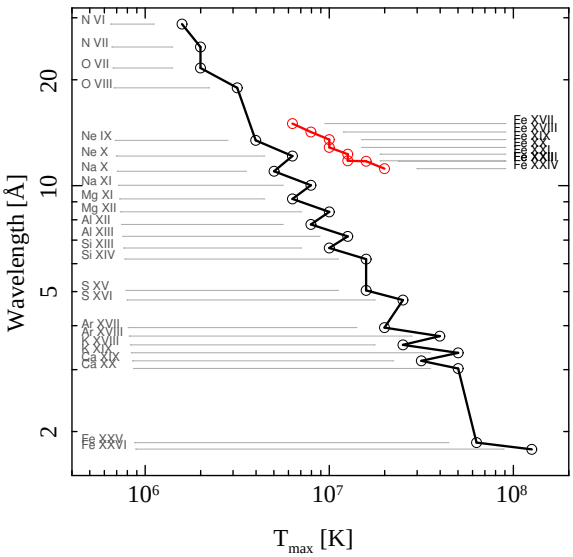

Figure 2. Over the wavelength range covered by HETG, the lines are sensitive to temperatures ranging from 1.5–60 MK. The circles mark the peak emissivity for prominent lines. The main diagonal (black) shows the H- and He-like lines. The Fe XVII–Fe XXIV lines are shown as a separate curve (red).

After we obtained a solution, we then ran several (∼100) Monte-Carlo iterations in which we perturbed the line fluxes by their uncertainties and then re-computed the emission measure distribution and abundances. This provided some idea of the uncertainty in the solution due to counting statistics. The 1σ envelopes are shown in the upper panel of Figure 3, though these do not represent independent errors. The uncertainties from counting statistics are relatively small. Especially for the abundances (see Figure 4), they are generally less than systematic uncertainties expected from the underlying atomic data.

For lines too weak or too few to include in the EMD reconstruction, we did post facto fits of their abundances by adopting the EMD as a frozen quantity, then fitted only the relevant abundance in narrow regions of the binned spectrum including the lines of interest. We did such for K XVIII, Na XI, and Al XIII. Abundance values are given in Table 2. We have also listed the Monte-Carlo determined statistical uncertainties, even if unrealistically small. A rough estimate of the minimum uncertainty from systematic errors is about 0.05–0.1 dex ($\sim 20\%$).

Since EMD reconstruction results can be dependent on methods, and since the emission measure and abundances are somewhat correlated, we had one final diagnostic which determines abundance ratios from linear combina-

Table 2
Elemental Abundances and FIP

Atom	FIP [eV]	AG89[a]	GS98[b]	Asp09[c]	Solar Coronal[d]	Solar Flares[e]	σ Gem	HR 1099
(1)	(2)	(3)	(4)	(5)	(6)	(7)	(8)	(9)
N	14.534	8.05	7.92	7.83	8.00	···	8.08 (0.03)	7.83 (0.03)
O	13.618	8.93	8.83	8.69	8.89	···	8.48 (0.01)	8.49 (0.01)
Ne	21.564	8.09	8.08	7.93	8.08	···	8.11 (0.01)	8.11 (0.01)
Na	5.139	6.33	6.33	6.24	6.93	···	5.92 (0.14)	6.07 (0.09)
Mg	7.646	7.58	7.58	7.60	8.15	···	6.97 (0.01)	6.91 (0.01)
Al	5.986	6.47	6.47	6.45	7.04	···	6.04 (0.06)	5.98 (0.06)
Si	8.151	7.55	7.55	7.51	8.10	7.48 (0.15)	6.94 (0.01)	6.87 (0.01)
S	10.360	7.21	7.33	7.12	7.27	6.84 (0.17)	6.57 (0.02)	6.53 (0.02)
Ar	15.759	6.56	6.40	6.40	6.58	6.45 (0.07)	6.48 (0.03)	6.37 (0.04)
K	4.341	5.12	5.12	5.03	5.67	5.86 (0.20)	5.63 (0.30)	$< \mathbf{5.44}$
Ca	6.113	6.36	6.36	6.34	6.93	···	6.21 (0.08)	6.11 (0.03)
Fe	7.870	7.67	7.50	7.50	8.10	7.91 (0.10)	6.87 (0.01)	6.81 (0.01)

Note. — Abundances are given on a logarithmic scale with $H = 12$. For convenience, we list several commonly used reference abundances (columns 3–6). Uncertainties on the stellar values (columns 8–9 in "()") are statistical, derived from the line fluxes, and do not include systematic uncertainties from atomic data, likely to be of order 10%.

[a] Anders & Grevesse (1989) photospheric solar values (default table for AtomDB (Smith et al. 2001; Foster et al. 2012)).

[b] Grevesse & Sauval (1998) photospheric solar values (default photospheric abundances in CHIANTI (Dere et al. 2009))

[c] Asplund et al. (2009)—recently determined, and preferred, photospheric solar abundances.

[d] Coronal abundances of Feldman et al. (1992), and of K from Landi, Feldman & Dere (2002) (a "coronal" table used in CHIANTI).

[e] Solar flare abundances from RESIK and RHESSI. Values in this column for Si, S, and Ar (with uncertainties) are from the re-analysis of spectra during the flare of 2002 December 26 (Figure 1, bottom). The K abundance is from the isothermal analysis of 20 flares (Sylwester et al. 2010b), and the Fe abundance from analysis of 20 RHESSI flares (Phillips & Dennis 2012).

Table 3
Temperature-Insensitive Abundance Ratios

Ratio	a_0	a_1	a_2	*TI*	*EMD*	*TI*	*EMD*
(1)	(2)	(3)	(4)	(5)	(6)	(7)	(8)
	Coefficients			σ Gem		HR 1099	
O:Mg	0.340	-6.519	1.687	0.7	1.3	0.2	1.7
Ne:O	2.214	1.386	-1.723	3.0	3.4	2.9	3.0
Ne:Mg	1.270	-0.611	2.980	3.8	4.3	4.2	5.1
Si:Mg	0.543	2.037	0.0097	1.1	1.0	1.1	1.0
Si:S	0.785	0.153	1.570	1.0	1.1	1.0	1.0
Ar:S	2.734	1.420	1.897	3.8	3.8	3.1	3.0

Note. — Abundance ratios are for abundances relative to solar photospheric. E.g., Ne:Mg means $(A_1/A_2) = [A(\mathrm{Ne})/A_\odot(\mathrm{Ne})]\,/\,[A(\mathrm{Mg})/A_\odot(\mathrm{Mg})]$. In columns 5–8, "*TI*" means the ratio was determined from "Temperature Insensitive" line ratios, whereas "*EMD*" refers to values from the emission measure distribution and abundance reconstruction. Values (and coefficients in colums 2 and 3) are referenced to Anders & Grevesse (1989). The ratios are derived from the fluxes of the H-like ($F_{i,H}$) and He-like ($F_{i,He}$) resonance lines for elements $i = 1, 2$ from the coefficients via $(A_1/A_2) = a_0(F_{1,\mathrm{H}} + a_1F_{1,\mathrm{He}})/(F_{2,\mathrm{H}} + a_2F_{2,\mathrm{He}})$.

tions of H- and He-like ion line fluxes. We refer to these as temperature-insensitive (TI) abundance ratios (see for example Liefke et al. 2008; García-Alvarez et al. 2005; Huenemoerder et al. 2009). With the exception of O:Mg, we obtained essentially the same abundance ratios from the EMD reconstruction as from the TI-method. We give the comparison in Table 3.

3.2. *RESIK Fitting and Modeling*

The fitting procedure for RESIK spectra, which as mentioned cover a much smaller range (3.4–6.05 Å) than the HETG spectra, follows that used in several previous analyses (Sylwester et al. 2010b; Sylwester, Sylwester & Phillips 2010; Sylwester et al. 2010a, 2012). The procedure is based on the CHIANTI database and software package (Dere et al. 2009) written in Interactive Data Language (IDL), widely used for solar x-ray and ultraviolet spectra, rather than the one used for HETG spectra (§ 3.1) which uses APEC and the AtomDB atomic database. Both CHIANTI and APEC databases draw on practically identical atomic data such as line excitation rates, giving (as we verified) indistinguishably different $G(T_e)$ functions for x-ray lines used in this analysis.

In previous analyses of RESIK spectra, the abundances of K, Ar, S, and Si were estimated from solar flare and active region spectra from the assumption that the line emission can be adequately described by an isothermal plasma with a characteristic temperature given by the ratio of the emission in the two wavelength channels of GOES. The lines are mostly emitted by H-like or He-like ions but also, in the case of S and Si, lower-temperature dielectronic lines emitted by the Li-like ions. For all the lines analyzed, values of the line flux divided by the volume emission measure plotted against temperature cluster about curves having the same temperature dependence as the theoretical $G(T_e)$ function for the line in question, as calculated from CHIANTI. The abundance is estimated by the amount the observational points have to be multiplied by to give the best fit to the $G(T_e)$ curve.

In recent, as yet unpublished, analysis of RESIK spectra, the isothermal assumption has been replaced by a method in which the EMD was derived by an iterative method re-

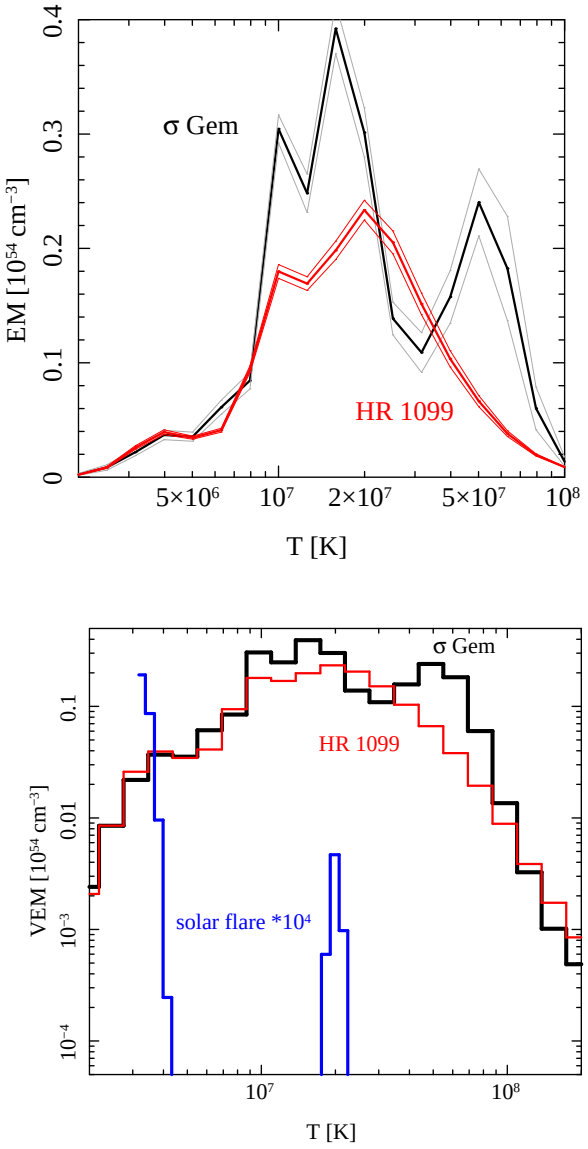

Figure 3. Top: Emission measure distributions for σ Gem (black) and HR 1099 (red), integrated over temperature bins of 0.1 dex. The upper and lower boundaries are statistical uncertainties due to line flux uncertainties, as determined from Monte-Carlo iteration. Bottom: The same emission measure distributions on a logarithmic scale over ranges to allow inclusion of the solar flare distribution corresponding to the spectrum shown in Figure 1 (blue) scaled up by a factor of 10^4.

lying on a Bayesian approach in which portions of each spectrum, including lines and continuum, were fit with a continuous function describing the EMD. This method, described by Sylwester, Schrijver & Mewe (1980), was used for the analysis of non-flaring active region RESIK spectra (Sylwester, Sylwester & Phillips 2010). The element abundances are free parameters. While it does not follow exactly the same method as that described for the wider-range HETG spectra in § 3.1, it is equivalent in that an EMD solution with enforced positivity and smoothness constraints are imposed with an iterative procedure to minimize χ^2 until convergence is achieved, i.e. the EMD describes the observed spectrum to within acceptable limits; the estimated abundances are the ones with the least value of χ^2. The RESIK spectrum shown in Figure 1 (bottom panel) integrated during the rise phase

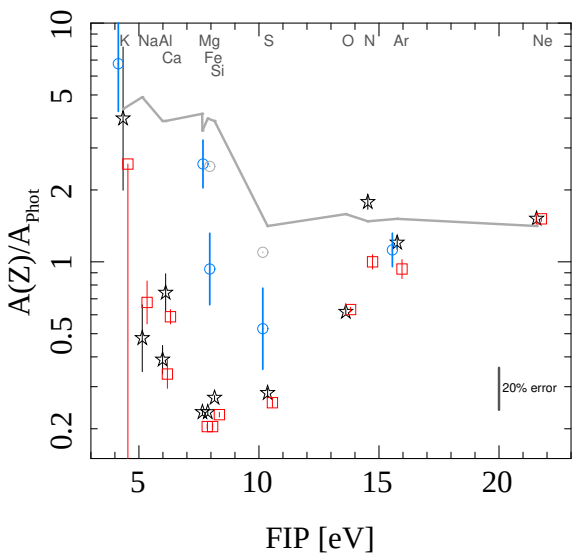

Figure 4. Abundances, relative to solar photospheric values of Asplund et al. (2009) for σ Gem (stars, black), and HR 1099 (squares, red, offset in FIP by $+0.2$ eV). Some error bars are unrealistically small, being based on emission line counting statistics; systematic uncertainties in atomic data and reconstruction methods would give about 20% uncertainties, as indicated by the representative error bar in the lower right. Values for the particular solar flare analyzed here are shown by circles (blue) for K, Fe, Si, S, and Ar, offset by -0.2 eV. The gray circles (without error bars) above the blue solar flare Si and S points are the isothermal-model values from prior analyses (see text, § 3.2). The solid gray line is the coronal to photospheric ratio, showing the FIP effect.

of the flare on 2002 December 26 was analyzed to give the EMD shown in Figure 3 (bottom panel); a nearly bimodal distribution resulted in this case, with emission centered on temperatures of ≈ 3 MK and ≈ 20 MK (other cases showed a more continuous distribution). This is the span of the $G(T_e)$ functions of the lines of the principal ions (from the Li-like Si satellites to the He-like K lines). The estimated abundances for Si, S, and Ar from this procedure using several spectra during the 2002 December 26 flare are given in Table 2 (column 7) and in Figure 4. The Ar abundance is similar to that from the isothermal assumption (Sylwester et al. 2010a), but S and Si abundances are less. The precise reason is under investigation, but it appears that the assumption of a single temperature to describe RESIK specra neglects the non-flaring active region component of the EMD which is of importance for the relatively low-temperature S and Si lines. The K abundance in Table 2 is from Sylwester et al. (2010b).

The Fe abundance in Table 2 is the average derived from RHESSI spectra during 20 flares given by Phillips & Dennis (2012).

3.3. *Densities, Timescales, and Validity of Coronal Ionization Equilibrium*

Solar and stellar flares are by definition highly dynamic events which undergo sudden heating, ionization, and recombination. Yet we have used plasma models in coronal ionization equilibrium (CIE), and this requires some justification. The ionization and recombination times are given by $\tau = 1/(N_e R)$ where R is the rate coefficient of ionization or recombination. Thus, τ is inversely proportional to N_e. For the HETG stellar spectra, we can estimate densities from the He-like triplet forbidden-to-intercombination line ratios. Testa, Drake & Peres (2004) provide values derived from the

Table 4
Electron Densities from He-like Triplet Ratios

Ion (1)	σ Gem[a] (2)	HR 1099[b] (3)	HR 1099[c] (4)
O VII	< 10.6	10.0 (0.6)	10.4 (0.2)
Ne IX	< 11.6[d]	···	< 10.9
	11.0 (0.55)[d]		
Mg XI	< 11.8	12.3 (0.1)	12.5 (0.5)

Note. — Values are common logarithms of densities in $[\mathrm{cm}^{-3}]$. The 1σ logarithmic uncertainties are given in parentheses.

[a] Values for σ Gem are from this work.
[b] Values from Testa, Drake & Peres (2004)
[c] Values from Ness et al. (2002)
[d] We give two values. The upper-limit used the emission-measure weighted line fluxes. If we assume all emission comes from the temperature of maximum emissivity, then the density is bounded, giving the second value.

same HR 1099 data studied here, and Ness et al. (2002) obtained similar values for HR 1099 from *XMM-Newton*/RGS spectra. Here we find comparable values for σ Gem, and we list them in Table 4 along with the prior determinations for HR 1099.

For the solar flare analyzed here, we have no direct density diagnostic, but we can be guided by previous measurements of similar flares. Doschek et al. (1981) used the O VII triplet in flare spectra obtained with the *P78-1* spacecraft to derive values of N_e reaching $10^{12}\,\mathrm{cm}^{-3}$ at flare maximum, declining to about $3\times10^{10}\,\mathrm{cm}^{-3}$ during the flare decay. Very similar densities during flares for the higher-temperature Fe XXI lines (maximum of $\sim\ 10^{12}\,\mathrm{cm}^{-3}$) were derived from the Solar Dynamics Observatory's EVE instrument by Milligan et al. (2012)). At temperatures observed during the RESIK flare, values of R for both ionizations and recombinations for ions of interest here range from $10^{-13}\,\mathrm{cm}^3\,\mathrm{s}^{-1}$ to $10^{-11}\,\mathrm{cm}^3\,\mathrm{s}^{-1}$, giving ionization and recombination times of less than $10\,\mathrm{s}$.

Hence, we can safely assume that over the scale of the *Chandra* stellar observations, and the relatively gradual changes in the observed light curves, that CIE is a reasonable assumption (a conclusion also reached by Testa et al. (2007), based on computations of timescales by Golub, Hartquist & Quillen (1989)). For solar flares similar to those seen by RESIK and RHESSI, densities of at least $10^{11}\,\mathrm{cm}^{-3}$ seem to apply, giving ionization and recombination times much less than the time scales of the observed temperature variations.

3.4. *Prior Results*

Our results are complementary to—but in some ways discrepant from—prior analysis of the same spectra. Drake et al. (2001) derived an emission measure and abundances for HR 1099, but were concerned primarily with relative abundances from modeling the strongest features. We obtain very similar abundance ratios. Their model, however, gives a poor representation of the observed spectrum in an absolute sense. Scaling their emission measure up by a factor of 8 and their abundances scaled down by a factor of 2.5 provides a reasonable match to observed counts above 5 Å, but is very poor at shorter wavelengths; this is probably due to their sharp cutoff in the EMD above $\sim 25\,\mathrm{MK}$.

Nordon & Behar (2007, 2008) analyzed flares in several stars, including σ Gem and HR 1099, using both *XMM-Newton* and *Chandra* spectra. The *XMM-Newton* spectra do not provide high resolution data at the short wavelengths of interest here; they relied on CCD resolution for lines of S, Ar, and Ca. Since the *XMM-Newton* observation of σ Gem was entirely of a flare state, they used the HETG σ Gem observation to represent its quiescent state. That is rather dubious now, given the strong, high-temperature peak in our EMD; the light curve was only slowly descending, while a very hot EMD component is typical of flares (see for examples Huenemoerder, Canizares & Schulz 2001; Güdel et al. 2004).

The EMD for σ Gem derived by Nordon & Behar (2008) is qualitatively similar to ours from 5–30 MK, but their high temperature peak from 50–100 MK is many times larger. This could simply represent the physical reality of an extremely large and hot flare in that observation. Our HR 1099 EMD shape is very similar to theirs as derived from *XMM-Newton* data, despite being observed at a different time from the *Chandra*/HETG spectra. For the same HETG observation of HR 1099 given in Nordon & Behar (2007), we have somewhat discrepant results: while our values for L_x, the x-ray luminosity over the 1–40 Å band, are of the same order ($10^{31}\,\mathrm{ergs\,s}^{-1}$), our integrated emission measure (VEM; see Table 1) is about 5 times larger. The shape of their EMD is also different, being broader and flatter. Our estimate of the VEM appears robust, being obtained even if fitting a single temperature plasma with uniformly variable abundances to a single order of one observation—the lines match poorly overall, but the continuum is a fair match and largely specifies the VEM. The factor of 5 difference is likely due to the abundances used. The line luminosity is degenerate in abundance and emission measure which enter as a product (see equations 1 and 2). Nordon & Behar (2007) were interested in abundances changes, and did not determine the Fe abundance. Hence, if one adopts an iron abundance 20% of solar in their analysis, their VEM would be 5 times larger.

Another case, which at first appears discrepant, actually agrees for the same reason. Sanz-Forcada, Brickhouse & Dupree (2002) derived the EMD for σ Gem and HR 1099 from UV emission lines. They also assumed solar abundances, and have a VEM about 5 times lower than our determination. If we use our model to predict the 135.85 Å Fe-blend flux, we obtain values within a factor of 2 of their measurements. If we use their model to evaluate the Fe XVII 15.01 Å flux, we get essentially the same as our measurement. Given that the stars are variable, we have very good agreement with the UV results.

In sum, we believe our models improve on—in a global and absolute sense—prior works which dealt with ratios, limited spectral ranges, or low resolution. Our detailed modeling is especially important for determining reliable values for some of the weak emission lines from low FIP elements, where the multi-thermal continuum model can be very important.

4. DISCUSSION

The origin of the values of elemental abundances in solar and stellar coronae is an unsolved problem. It is an important one because the differences in abundances from the underlying photosphere could provide information on the coronal structure, such as loop geometry or Alfvén wave frequency and amplitude, e.g., under the ponderomotive fractionation theory of Laming (2012); Laming & Hwang (2009). Or if the relation between coronal and photospheric abundances were

known, then x-ray spectra would be very valuable in determining abundances in star-forming regions where stars are deeply embedded and not visible in other wavelength bands.

The x-ray spectral modeling is fairly simple; the spectra are amenable to determination of absolute abundances, especially in the short wavelength region where the continuum is dominated by a single temperature, and the line-to-continuum ratio is directly proportional to the elemental abundance. At about 10 MK, the continuum flux at 3 Å is about 10% that at 6 Å, but becomes comparable by about 30 MK. Our model for σ Gem shows that below 6 Å the primary contribution is from plasmas with $T \sim 50$ MK, and 90% of the continuum is emitted by H and He thermal bremsstrahlung. Above 6 Å, the continuum comes from plasmas with temperatures which differ by more than 0.3 dex—the typical width of a line emissivity or $G(T)$ function—which means that a multi-thermal plasma model is required to interpret the line-to-continuum ratio in terms of an absolute abundance. Hence, one must use all the lines available and perform emission measure and abundance reconstructions.

The region below 6 Å fortunately contains lines from abundant elements of both high and low FIP, in particular K (3.35 Å; $FIP = 4.34$ eV) and Ca (3.0, 3.2 Å; 6.11 eV), and at the other extreme, Ar (3.7, 3.9 Å; 15.76 eV). Hence, these abundance values are reliable and can be compared to the solar flare values.

Of primary interest are the species with the two lowest FIPs, K and Na, which have not previously been measured in these stars. The K XVIII He-like triplet (3.54 Å) was marginally detected in σ Gem, but is only an upper limit in HR 1099. The Na abundance was determined from the H-like Na XI (10.02 Å) line, whose spectral region is crowded and contains some unidentified lines (probably due to Fe), but the feature is detected at the right wavelength for Na XI. It has been seen in other coronally active stars at about the same strength (García-Alvarez et al. 2005; Sanz-Forcada, Maggio & Micela 2003). We show detail for these regions in Figures 5 and 6.

In the HETG spectra, we have strong and well modeled Fe XXV emission (1.85 Å). The Fe abundance is also constrained by lower ionization states at longer wavelengths and lower temperatures, and appears to be robust. Emission lines from Mg, Al, Ne, O, and Ca are also present, and so we have derived their respective abundances. In Figure 7 we show a portion of the σ Gem spectrum covering a number of elements and ions to display the quality of the fit. The HR 1099 spectrum and model are of similar quality.

We show all the stellar abundances we have been able to measure in Figure 4, referenced to the solar photospheric values of Asplund et al. (2009). It appears that the abundance of K in σ Gem is near the solar coronal value; that is, it is enhanced well above the solar photospheric value. Na, however, is much depleted, as are the other low-FIP (< 10 eV) elements, only attaining solar photospheric abundances (or greater) at high FIP for N, Ar, and Ne. In HR 1099, K was not detected and the upper limit is at about 2.6 times photospheric. Otherwise, σ Gem and HR 1099 have very similar abundances. The important Ne:O ratio is found to be nearly identical in σ Gem and HR 1099 at 0.42, as was found for HR 1099 by Drake & Testa (2005).

As is typical for coronally active stars, there is no solar-like FIP effect in which where all low-FIP elements are over-abundant relative to the photosphere by about a factor of 4. Instead, we see very sub-solar abundances, except for K, N, Ar, and Ne.

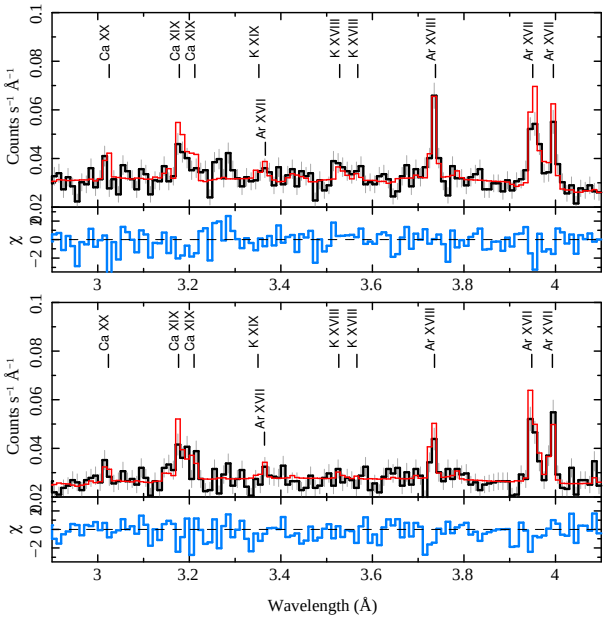

Figure 5. Detail of the K XVIII region; Top: σ Gem; bottom: HR 1099. Scales are the same in each panel. Black is the observed spectrum, red is the convolved model, error bars are in gray, and below each spectrum are $\delta\chi$ residuals (in blue).

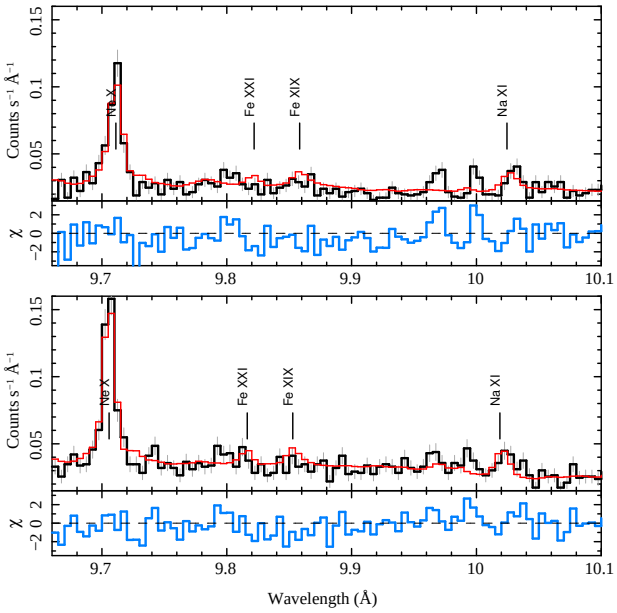

Figure 6. Detail of the Na XI region; Top: σ Gem; bottom: HR 1099. Scales are the same in each panel. Black is the observed spectrum, red is the convolved model, error bars are in gray, and below each spectrum are $\delta\chi$ residuals (in blue). There are no identifications for the two features just blue-ward of Na XI. The strongest feature in the region is from Ne X H-Lyγ (9.708 Å).

The Sun also shows reduced Si and S in the 2002 December 26 flare (blue circles in Figure 4); mean values obtained from many flares (though under an isothermal assumption) are higher (gray circles). Abundances of Ar and K for the 2002 December 26 flare showed no difference from the mean. Details of the solar flare abundance determination variance—we have 2795 spectra in various phases of 20 flares—can be

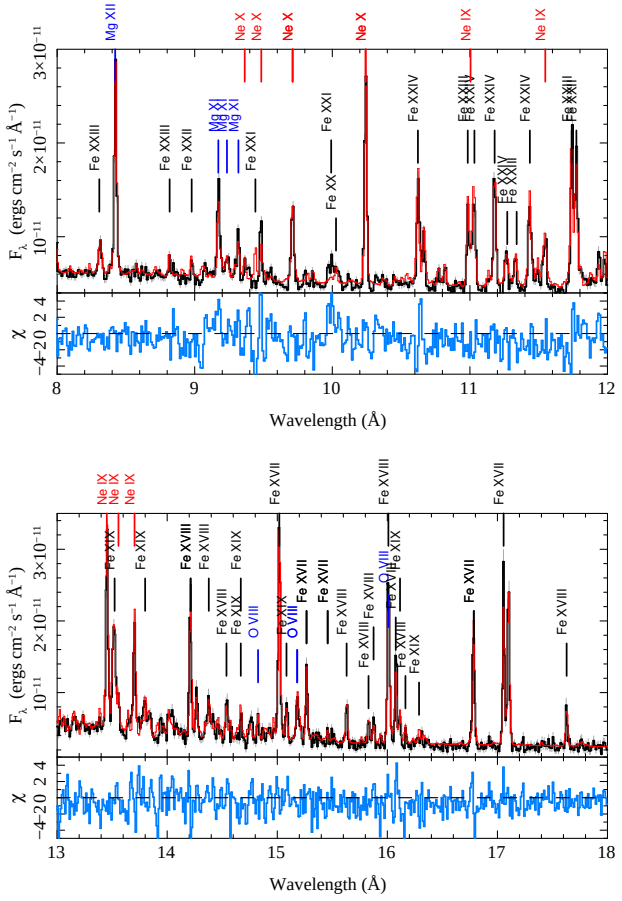

Figure 7. Here we show the MEG spectra and models for the 8–12 Å and 13–18 Å regions of σ Gem. Flux-corrected spectra are in black, red is the model convolved by the instrumental resolution, and below each, in blue, are residuals. Line identifications for the strongest emission lines in the regions are given. In addition to lines from multiple ions of Fe, there are the Mg XII resonance line (8.42 Å) and Mg XI He-like triplet (9.17, 9.23, 9.31 Å), Ne X lines at 10.24, 9.78, 9.38, and 9.36 Å, the Ne IX He-like triplet at 13.45, 13.55, and 13.70 Å, and O VIII lines at 15.176 and 16.01 Å (blended strongly with Fe XVIII). The quality of the HR 1099 fit is similar.

Figure 8. The light curve of σ Gem derived from the *Chandra*/HETGS dispersed spectrum, summed over HEG and MEG orders ±1. There were two separate observations made with *Chandra*/HETGS, each lasting about 60 ks and separated by about 50 ks. The total band (upper black) is 1.7–25 Å, a hard band (blue) is 1.7–8.0 Å, and soft (red) is 10–25 Å. In the lower panel is a hardness ratio derived from the hard and soft band light curves. The decrease in hardness coincident with decreasing rate (proportional to emission measure) is indicative of cooling flares.

found in the series of papers cited above (see § 3.2).

Both σ Gem and HR 1099 were in flaring states during the HETG observations. Light curves for the *Chandra* HR 1099 data can be found in Ayres et al. (2001) and Nordon & Behar (2007). In Figure 8 we show the σ Gem light curve derived from the dispersed spectral photon lists. While there is no flare rise seen over the times of the two HETGS exposures, the count rate decays steadily over the two days of observations from about 3.8 counts s^{-1} to 3.0 counts s^{-1}, and the spectrum softens as seen in a hardness ratio. This fading and cooling, combined with the strong, hot EMD peak, suggest that the star is in the late stages of a large flare.

5. CONCLUSIONS

Our primary goal in this work was to compare low and high FIP elemental abundances in the Sun and stars using x-ray spectra of similar high-resolution and bandpass. Such was possible using the RESIK instrument for the Sun, and the *Chandra*/HETGS for stars. In order to obtain results for the lowest FIP element present (K), we required the highest fluence HETGS coronal spectra, which were of σ Gem and HR 1099. In order to have some basis for comparison of the Sun to stars, we used a solar flare spectrum so that it has plasma at comparable temperatures to the stars.

As a secondary goal, the richness of the HETGS spectra allowed determination of elemental abundances for other low FIP species, namely Na, Al, and Ca, which had not before been measured in detail, as well as measurements for the high-FIP elements, O, N, and Ne.

Determination of the stellar abundances from the broader HETGS spectrum necessarily required a full emission measure solution, since emission measure and abundance appear as a factor in line flux formation, and because the continuum beyond about 6 Å has significant contributions from a broad range of temperatures. These details must be considered carefully when attempting comparisions to other work.

Hence, we have determined new elemental abundances for the lowest FIP species—particularly K and Na, but also Ca and Al—in two stellar coronal sources with very hot, flaring plasmas. While the abundance of K (having the lowest FIP) in σ Gem is similar to that in the solar corona, other low-FIP elements (Na, Al, Ca, Mg, Fe, and Si) are strongly depleted, only becoming near or above solar for the high FIP elements N, Ar, and Ne. Even the stellar S abundances (considered high-FIP) has a very low relative abundance.

Except for K, for which we only have an upper-limit in HR 1099, the two stellar elemental abundance distributions are remarkably similar to each other, despite differences in their rotational periods (2.8 d and 19.6 d for HR 1099 and σ Gem, respectively) and luminosity classes.

The solar flare plasma, which reaches stellar coronal temperatures of 20 MK, shows low-FIP elements of K and Fe to be typical of the solar corona (that is, enhanced relative to photospheric values), while Si and S are photospheric or lower, but still above the stellar values. The abundances of Ar is similar in the solar and stellar flares. The overall trend with

FIP is similar to, but less extreme than the stellar case, with the exception of Fe having high relative abundance, though it has about the same FIP as Si.

Both the stellar and solar cases show abundance trends more complicated than simple FIP or "inverse"-FIP during flares. Whether other active stars have similar patterns at the lowest FIP would require investment of 100-200 ks per star to raise some of the existing lower fluence HETGS observations of coronal sources to comparable levels. Likewise, further solar flare analysis is required to determine whether the Fe and Si abundances are always so different, or whether the solar trend sometimes mimics the stellar trend more closely.

Acknowledgements: Support for this work was provided by the National Aeronautics and Space Administration through the Smithsonian Astrophysical Observatory contract SV3-73016 to MIT for Support of the Chandra X-Ray Center, which is operated by the Smithsonian Astrophysical Observatory for and on behalf of the National Aeronautics Space Administration under contract NAS8-03060 (DPH). We also gratefully acknowledge financial support from the Polish Ministry of Education and Science (Grant 2011/01/B/ST9/05861), the European Commissions Seventh Framework Programme (FP7/2007-2013) under the grant agreement eHEROES (project no. 284461), and the UK Royal Society/Polish Academy of Sciences International Joint Project for travel support. The RESIK spectra were analyzed with CHIANTI which is a collaborative project involving George Mason University, the University of Michigan, and the University of Cambridge.

Facilities: CXO (HETG/ACIS), *CORONAS-F* (RESIK)

REFERENCES

Anders, E., & Grevesse, N., 1989, Geochim. Cosmochim. Acta, 53, 197
Asplund, M., Grevesse, N., Sauval, A. J., & Scott, P., 2009, ARA&A, 47, 481
Audard, M., Güdel, M., & Mewe, R., 2001, A&A, 365, L318
Ayres, T. R., Brown, A., Osten, R. A., Huenemoerder, D. P., Drake, J. J., Brickhouse, N. S., & Linsky, J. L., 2001, ApJ, 549, 554
Brinkman, A. C., et al., 2001, A&A, 365, L324
Canizares, C. R., et al., 2005, PASP, 117, 1144
Davis, J. E., 2001, ApJ, 548, 1010
Dere, K. P., Landi, E., Young, P. R., Del Zanna, G., Landini, M., & Mason, H. E., 2009, A&A, 498, 915
Doschek, G. A., Feldman, U., Landecker, P. B., & McKenzie, D. L., 1981, ApJ, 249, 372
Drake, J. J., Brickhouse, N. S., Kashyap, V., Laming, J. M., Huenemoerder, D. P., Smith, R., & Wargelin, B. J., 2001, ApJ, 548, L81
Drake, J. J., & Testa, P., 2005, Nature, 436, 525
Eker, Z., et al., 2008, MNRAS, 389, 1722
Feldman, U., 1992, Phys. Scr, 46, 202
Feldman, U., & Laming, J., 2000, Phys. Scr, 61, 222
Feldman, U., Mandelbaum, P., Seely, J. F., Doschek, G. A., & Gursky, H., 1992, ApJS, 81, 387
Foster, A. R., Ji, L., Smith, R. K., & Brickhouse, N. S., 2012, ApJ, 756, 128
Fruscione, A., et al., 2006, in SPIE Conference Series, Vol. 6270
Güdel, M., Audard, M., Reale, F., Skinner, S. L., & Linsky, J. L., 2004, A&A, 416, 713
García-Alvarez, D., Drake, J. J., Lin, L., Kashyap, V. L., & Ball, B., 2005, ApJ, 621, 1009
Golub, L., Hartquist, T. W., & Quillen, A. C., 1989, Sol. Phys., 122, 245
Grevesse, N., & Sauval, A. J., 1998, Space Science Reviews, 85, 161
Huenemoerder, D. P., Canizares, C. R., Drake, J. J., & Sanz-Forcada, J., 2003, ApJ, 595, 1131
Huenemoerder, D. P., Canizares, C. R., & Schulz, N. S., 2001, ApJ, 559, 1135
Huenemoerder, D. P., Schulz, N. S., Testa, P., Kesich, A., & Canizares, C. R., 2009, ApJ, 707, 942
Jordan, C., 1975, MNRAS, 170, 429
Kaastra, J. S., Mewe, R., Liedahl, D. A., Singh, K. P., White, N. E., & Drake, S. A., 1996, A&A, 314, 547
Laming, J. M., 2012, ApJ, 744, 115
Laming, J. M., & Hwang, U., 2009, ApJ, 707, L60
Landi, E., Feldman, U., & Dere, K. P., 2002, ApJS, 139, 281
Lemen, J. R., Mewe, R., Schrijver, C. J., & Fludra, A., 1989, ApJ, 341, 474
Liefke, C., Fuhrmeister, B., & Schmitt, J. H. M. M., 2010, A&A, 514, A94
Liefke, C., Ness, J. ., Schmitt, J. H. M. M., & Maggio, A., 2008, A&A, 491, 859
Mazzotta, P., Mazzitelli, G., Colafrancesco, S., & Vittorio, N., 1998, A&AS, 133, 403
Milligan, R. O., Kennedy, M. B., Mathioudakis, M., & Keenan, F. P., 2012, ApJ, 755, L16
Ness, J.-U., Schmitt, J. H. M. M., Burwitz, V., Mewe, R., Raassen, A. J. J., van der Meer, R. L. J., Predehl, P., & Brinkman, A. C., 2002, A&A, 394, 911
Nordon, R., & Behar, E., 2007, A&A, 464, 309
Nordon, R., & Behar, E., 2008, A&A, 482, 639
Phillips, K. J. H., & Dennis, B. R., 2012, ApJ, 748, 52
Phillips, K. J. H., Sylwester, J., Sylwester, B., & Kuznetsov, V. D., 2010, ApJ, 711, 179
Pottasch, S. R., 1963, ApJ, 137, 945
Sanz-Forcada, J., Brickhouse, N. S., & Dupree, A. K., 2002, ApJ, 570, 799
Sanz-Forcada, J., Maggio, A., & Micela, G., 2003, A&A, 408, 1087
Smith, R. K., Brickhouse, N. S., Liedahl, D. A., & Raymond, J. C., 2001, ApJ, 556, L91
Strassmeier, K. G., 2009, A&A Rev., 17, 251
Sylwester, B., Sylwester, J., & Phillips, K. J. H., 2010, A&A, 514, A82
Sylwester, J., et al., 2005, Sol. Phys., 226, 45
Sylwester, J., Schrijver, J., & Mewe, R., 1980, Sol. Phys., 67, 285
Sylwester, J., Sylwester, B., Phillips, K. J. H., & Kuznetsov, V. D., 2010a, ApJ, 720, 1721
Sylwester, J., Sylwester, B., Phillips, K. J. H., & Kuznetsov, V. D., 2010b, ApJ, 710, 804
Sylwester, J., Sylwester, B., Phillips, K. J. H., & Kuznetsov, V. D., 2012, ApJ, 751, 103
Testa, P., Drake, J. J., & Peres, G., 2004, ApJ, 617, 508
Testa, P., Drake, J. J., Peres, G., & Huenemoerder, D. P., 2007, ApJ, 665, 1349
van Leeuwen, F., 2007, A&A, 474, 653
Wood, B. E., Laming, J. M., & Karovska, M., 2012, ApJ, 753, 76
Wood, B. E., & Linsky, J. L., 2010, ApJ, 717, 1279

Table 5
σ Gem Line Measurements

Ion	$\log T_{\max}$[a]	λ_0[b]	$\lambda_{\rm obs}$[c]	f[d]	$f_{\rm model}$[e]
	log [K]	[Å]	[Å (m Å)]	[10^{-6} phot cm^{-2} s^{-1}]	
(1)	(2)	(3)	(4)	(5)	(6)
Fe XXV	7.82	1.8607	1.858 (1.4)	83.4 (8.0)	68.5
Ca XIX	7.50	3.1772	3.176 (2.0)	16.8 (3.2)	13.5
Ca XIX	7.46	3.1909	3.192 (3.6)	9.8 (2.9)	4.4
Ca XIX	7.46	3.2110	3.210 (3.4)	7.4 (2.5)	4.5
K XVIII	7.42	3.5273	3.521 (5.2)	6.8 (2.5)	0.8
K XVIII	7.36	3.5434	3.545 (0.0)	2.3 (2.3)	0.1
K XVIII	7.39	3.5669	3.568 (0.0)	6.0 (2.5)	0.4
Ar XVIII	7.73	3.7338	3.736 (0.7)	28.4 (2.9)	29.5
Ar XVII	7.36	3.9491	3.950 (0.6)	38.7 (3.4)	36.8
Ar XVII	7.31	3.9676	3.968 (1.1)	17.8 (2.9)	10.0
S XVI	7.51	3.9923	3.995 (0.9)	25.1 (3.0)	11.8
S XVI	7.57	4.7301	4.731 (0.6)	47.3 (3.8)	52.4
Si XIV	7.43	4.9462	4.948 (1.9)	8.4 (2.9)	4.3
S XV	7.20	5.0387	5.041 (0.5)	58.4 (4.2)	56.3
S XV	7.16	5.0648	5.068 (2.0)	13.2 (3.2)	12.8
S XV	7.17	5.1015	5.101 (1.0)	31.3 (3.7)	24.7
Si XIV	7.42	5.2174	5.220 (0.9)	26.2 (3.8)	24.1
Si XIII	7.07	5.6805	5.685 (1.3)	17.1 (3.1)	16.9
Si XIV	7.40	6.1831	6.185 (0.2)	162.5 (3.9)	164.8
Si XIII	7.03	6.6479	6.651 (0.2)	125.5 (3.5)	120.2
Si XIII	6.99	6.6866	6.690 (0.6)	26.8 (2.4)	22.9
Si XIII	7.00	6.7403	6.742 (0.3)	82.0 (2.9)	58.2
Mg XII	7.22	7.1063	7.109 (0.6)	26.7 (2.3)	30.6
Al XIII	7.38	7.1714	7.172 (0.7)	30.0 (2.4)	29.0
Al XII	6.94	7.7573	7.761 (1.1)	16.1 (2.0)	8.8
Mg XI	6.87	7.8503	7.853 (1.3)	12.3 (2.1)	11.5
Fe XXIV	7.46	7.9857	7.986 (0.9)	22.2 (2.4)	19.0
Fe XXIV	7.46	7.9960	7.998 (1.1)	12.3 (2.4)	9.5
Fe XXIII	7.28	8.3038	8.307 (1.3)	17.8 (3.2)	19.4
Fe XXIV	7.44	8.3161	8.320 (0.9)	26.4 (3.4)	19.1
Fe XXIV	7.44	8.3761	8.378 (2.0)	9.0 (2.5)	7.7
Mg XII	7.19	8.4219	8.424 (0.2)	202.8 (5.3)	208.2
Fe XXI	7.10	8.5740	8.578 (1.2)	13.3 (2.3)	11.2
Fe XXIII	7.27	8.8149	8.819 (0.8)	24.0 (2.5)	22.0
Fe XXII	7.17	8.9748	8.979 (0.8)	21.2 (2.4)	20.8
Mg XI	6.84	9.1687	9.172 (0.3)	112.1 (4.1)	79.0
Fe XXI	7.10	9.1944	9.192 (1.9)	20.4 (2.9)	8.4
Mg XI	6.80	9.2297	9.233 (1.3)	19.7 (2.8)	12.7
Mg XI	6.81	9.3143	9.318 (0.4)	56.5 (3.1)	39.5
Ne X	6.99	9.4808	9.481 (0.4)	64.0 (2.7)	38.9
Fe XIX	6.97	9.6951	9.698 (2.7)	18.1 (3.8)	7.6
Ne X	6.98	9.7082	9.712 (0.7)	90.5 (4.8)	89.7
Na XI	7.08	10.0240	10.031 (1.0)	26.9 (3.1)	23.2
Ni XIX	6.87	10.1100	10.112 (4.0)	9.7 (4.7)	3.9
Ne X	6.97	10.2390	10.242 (0.0)	260.3 (6.2)	252.8
Fe XXIV	7.45	10.6190	10.625 (0.5)	145.8 (5.4)	134.3
Fe XXIV	7.45	10.6630	10.665 (0.5)	69.9 (4.2)	69.4
Fe XIX	6.97	10.8160	10.823 (1.0)	29.3 (3.3)	27.1
Fe XXIII	7.27	10.9810	10.985 (0.0)	93.1 (4.8)	104.8
Ne IX	6.66	11.0010	11.005 (1.5)	35.6 (4.2)	22.1
Fe XXIII	7.27	11.0190	11.024 (1.0)	76.3 (7.2)	67.2
Fe XXIV	7.42	11.0290	11.036 (0.5)	72.9 (7.3)	88.3
Fe XVII	6.76	11.1310	11.138 (2.0)	18.9 (3.8)	19.8
Fe XXIV	7.42	11.1760	11.179 (0.0)	166.7 (6.7)	159.2
Fe XVII	6.76	11.2540	11.255 (1.5)	24.6 (4.9)	27.4
Fe XXIV	7.42	11.2680	11.268 (1.0)	46.9 (5.2)	36.5
Fe XVIII	6.89	11.3260	11.330 (0.5)	48.1 (4.0)	38.7
Fe XVIII	6.88	11.5270	11.531 (1.0)	48.9 (4.4)	37.8
Ne IX	6.64	11.5440	11.551 (0.5)	68.7 (4.8)	63.6
Fe XXIII	7.26	11.7360	11.744 (0.5)	238.8 (7.4)	223.9
Fe XXII	7.16	11.7700	11.775 (0.0)	209.9 (7.0)	188.6
Fe XXII	7.15	11.9320	11.937 (1.0)	65.7 (4.9)	27.2
Ne X	6.94	12.1350	12.137 (3.5)	1839.0 (19.3)	1838.2
Fe XXIII	7.25	12.1610	12.162 (1.0)	120.4 (9.2)	119.6
Fe XVII	6.75	12.2660	12.268 (1.0)	70.9 (9.7)	60.0
Fe XXI	7.09	12.2840	12.289 (0.5)	304.5 (12.2)	342.4
Fe XXII	7.15	12.7540	12.756 (0.5)	79.9 (6.6)	64.5
Fe XX	7.03	12.8240	12.831 (1.0)	140.1 (10.0)	60.1
Fe XX	7.03	12.8460	12.849 (1.0)	123.9 (14.1)	140.4
Fe XX	7.03	13.3850	13.381 (2.0)	47.1 (9.2)	33.0
Fe XIX	6.96	13.4230	13.434 (2.5)	42.2 (7.9)	24.1
Ne IX	6.61	13.4470	13.452 (0.5)	414.6 (14.3)	443.3
Fe XIX	6.96	13.4620	13.471 (1.0)	92.5 (8.7)	55.8

Table 5 — *Continued*

Ion	$\log T_{\rm max}$[a] log [K]	λ_0[b] [Å]	$\lambda_{\rm obs}$[c] [Å (m Å)]	f[d] [10^{-6} phot cm^{-2} s^{-1}]	$f_{\rm model}$[e]
(1)	(2)	(3)	(4)	(5)	(6)
Fe XIX	6.96	13.5180	13.527 (0.5)	188.4 (12.1)	211.4
Ne IX	6.58	13.5520	13.558 (1.0)	101.5 (9.2)	71.7
Fe XIX	6.96	13.6450	13.654 (1.5)	55.9 (6.9)	33.8
Ne IX	6.59	13.6990	13.703 (0.5)	279.7 (11.5)	249.3
Fe XX	7.02	13.7670	13.771 (2.5)	54.8 (7.3)	23.2
Fe XIX	6.96	13.7950	13.800 (1.0)	102.6 (8.6)	90.1
Fe XVIII	6.87	14.2080	14.209 (0.5)	309.1 (14.3)	387.5
Fe XVIII	6.87	14.2560	14.263 (1.0)	87.1 (7.1)	76.7
Fe XX	7.02	14.2670	14.276 (1.5)	54.0 (12.1)	39.3
Fe XVIII	6.87	14.3430	14.350 (1.5)	52.1 (7.9)	43.0
Fe XVIII	6.87	14.3730	14.379 (1.0)	112.8 (10.0)	92.5
Fe XVIII	6.87	14.5340	14.541 (1.0)	115.8 (12.8)	76.8
Fe XIX	6.96	14.6640	14.671 (1.0)	72.4 (9.6)	85.0
O VIII	6.71	14.8210	14.823 (1.0)	60.4 (8.5)	46.9
Fe XVII	6.73	15.0140	15.017 (0.5)	542.6 (18.0)	563.4
Fe XIX	6.95	15.0790	15.085 (1.0)	118.9 (9.5)	87.4
O VIII	6.70	15.1760	15.180 (1.0)	118.1 (9.3)	106.7
Fe XIX	6.96	15.1980	15.205 (1.5)	49.5 (7.5)	54.5
Fe XVII	6.72	15.2610	15.266 (0.5)	190.4 (10.8)	174.6
Fe XVII	6.70	15.4530	15.459 (2.0)	32.7 (6.9)	28.8
Fe XVIII	6.87	15.4940	15.493 (3.0)	20.2 (6.4)	9.4
Fe XVIII	6.86	15.6250	15.629 (1.0)	96.0 (9.2)	118.6
Fe XVIII	6.86	15.8240	15.829 (1.5)	58.2 (8.5)	71.0
Fe XVIII	6.86	15.8700	15.876 (1.0)	67.3 (8.9)	42.8
Fe XVIII	6.86	16.0710	16.079 (0.5)	244.5 (14.2)	199.9
Fe XIX	6.95	16.1100	16.112 (1.0)	75.9 (9.8)	92.6
Fe XVIII	6.87	16.1590	16.169 (2.0)	35.9 (8.0)	52.1
Fe XVII	6.70	16.7800	16.781 (0.5)	328.9 (17.7)	351.5
Fe XVII	6.71	17.0510	17.056 (0.5)	443.8 (21.3)	413.6
Fe XVII	6.70	17.0960	17.101 (0.5)	470.2 (21.8)	476.8
Fe XVIII	6.86	17.6230	17.627 (1.5)	108.1 (13.9)	121.7
O VII	6.38	17.7680	17.758 (5.5)	19.0 (9.8)	13.2
O VII	6.37	18.6270	18.633 (2.0)	74.1 (14.1)	37.3
Ca XVIII	7.07	18.6910	18.685 (5.5)	18.8 (11.5)	25.5
O VIII	6.65	18.9700	18.974 (0.0)	2142.0 (60.9)	2140.0
Ca XVIII	7.03	19.6420	19.627 (15.0)	8.1 (10.8)	18.2
Ca XVIII	7.03	19.7950	19.793 (8.5)	16.2 (13.5)	36.3
N VII	6.55	19.8260	19.830 (5.5)	35.5 (15.8)	29.6
N VII	6.53	20.9100	20.912 (3.0)	103.8 (23.7)	99.6
O VII	6.34	21.6020	21.605 (2.0)	212.8 (32.5)	247.0
O VII	6.32	21.8020	21.815 (8.5)	41.4 (22.4)	35.3
O VII	6.32	22.0980	22.101 (2.0)	211.5 (37.1)	155.1
N VII	6.49	24.7820	24.785 (1.0)	707.4 (62.0)	667.3

Note. — Lines used in the EMD and abundance reconstruction for σ Gem.

[a] $T_{\rm max}$ is the temperature of maximum emissivity according to AtomDB (Smith et al. 2001; Foster et al. 2012).

[b] The theoretical wavelength, from AtomDB.

[c] The measured wavelength; 1σ uncertainties are in parentheses in units of mÅ.

[d] The measured line flux; 1σ uncertainties are in parentheses.

[e] The theoretical line flux, from AtomDB, for the derived EMD and abundance model.

Table 6
HR 1099 Line Measurements

Ion	$\log T_{\max}$	λ_0	$\lambda_{\rm obs}$	f	$f_{\rm model}$
	log [K]	[Å]	[Å(m Å)]	[10^{-6} phot cm^{-2} s^{-1}]	
(1)	(2)	(3)	(4)	(5)	(6)
Fe XXV	7.82	1.8607	1.858 (1.4)	83.4 (8.0)	68.5
Ca XIX	7.50	3.1772	3.176 (2.0)	16.8 (3.2)	13.5
Ca XIX	7.46	3.1909	3.192 (3.6)	9.8 (2.9)	4.4
Ca XIX	7.46	3.2110	3.210 (3.4)	7.4 (2.5)	4.5
K XVIII	7.42	3.5273	3.521 (5.2)	6.8 (2.5)	0.8
K XVIII	7.36	3.5434	3.545 (0.0)	2.3 (2.3)	0.1
K XVIII	7.39	3.5669	3.568 (0.0)	6.0 (2.5)	0.4
Ar XVIII	7.73	3.7338	3.736 (0.7)	28.4 (2.9)	29.5
Ar XVII	7.36	3.9491	3.950 (0.6)	38.7 (3.4)	36.8
Ar XVII	7.31	3.9676	3.968 (1.1)	17.8 (2.9)	10.0
S XVI	7.51	3.9923	3.995 (0.9)	25.1 (3.0)	11.8
S XVI	7.57	4.7301	4.731 (0.6)	47.3 (3.8)	52.4
Si XIV	7.43	4.9462	4.948 (1.9)	8.4 (2.9)	4.3
S XV	7.20	5.0387	5.041 (0.5)	58.4 (4.2)	56.3
S XV	7.16	5.0648	5.068 (2.0)	13.2 (3.2)	12.8
S XV	7.17	5.1015	5.101 (1.0)	31.3 (3.7)	24.7
Si XIV	7.42	5.2174	5.220 (0.9)	26.2 (3.8)	24.1
Si XIII	7.07	5.6805	5.685 (1.3)	17.1 (3.1)	16.9
Si XIV	7.40	6.1831	6.185 (0.2)	162.5 (3.9)	164.8
Si XIII	7.03	6.6479	6.651 (0.2)	125.5 (3.5)	120.2
Si XIII	6.99	6.6866	6.690 (0.6)	26.8 (2.4)	22.9
Si XIII	7.00	6.7403	6.742 (0.3)	82.0 (2.9)	58.2
Mg XII	7.22	7.1063	7.109 (0.6)	26.7 (2.3)	30.6
Al XIII	7.38	7.1714	7.172 (0.7)	30.0 (2.4)	29.0
Al XII	6.94	7.7573	7.761 (1.1)	16.1 (2.0)	8.8
Mg XI	6.87	7.8503	7.853 (1.3)	12.3 (2.1)	11.5
Fe XXIV	7.46	7.9857	7.986 (0.9)	22.2 (2.4)	19.0
Fe XXIV	7.46	7.9960	7.998 (1.1)	12.3 (2.4)	9.5
Fe XXIII	7.28	8.3038	8.307 (1.3)	17.8 (3.2)	19.4
Fe XXIV	7.44	8.3161	8.320 (0.9)	26.4 (3.4)	19.1
Fe XXIV	7.44	8.3761	8.378 (2.0)	9.0 (2.5)	7.7
Mg XII	7.19	8.4219	8.424 (0.2)	202.8 (5.3)	208.2
Fe XXI	7.10	8.5740	8.578 (1.2)	13.3 (2.3)	11.2
Fe XXIII	7.27	8.8149	8.819 (0.8)	24.0 (2.5)	22.0
Fe XXII	7.17	8.9748	8.979 (0.8)	21.2 (2.4)	20.8
Mg XI	6.84	9.1687	9.172 (0.3)	112.1 (4.1)	79.0
Fe XXI	7.10	9.1944	9.192 (1.9)	20.4 (2.9)	8.4
Mg XI	6.80	9.2297	9.233 (1.3)	19.7 (2.8)	12.7
Mg XI	6.81	9.3143	9.318 (0.4)	56.5 (3.1)	39.5
Ne X	6.99	9.4808	9.481 (0.4)	64.0 (2.7)	38.9
Fe XIX	6.97	9.6951	9.698 (2.7)	18.1 (3.8)	7.6
Ne X	6.98	9.7082	9.712 (0.7)	90.5 (4.8)	89.7
Na XI	7.08	10.0240	10.031 (1.0)	26.9 (3.1)	23.2
Ni XIX	6.87	10.1100	10.112 (4.0)	9.7 (4.7)	3.9
Ne X	6.97	10.2390	10.242 (0.0)	260.3 (6.2)	252.8
Fe XXIV	7.45	10.6190	10.625 (0.5)	145.8 (5.4)	134.3
Fe XXIV	7.45	10.6630	10.665 (0.5)	69.9 (4.2)	69.4
Fe XIX	6.97	10.8160	10.823 (1.0)	29.3 (3.3)	27.1
Fe XXIII	7.27	10.9810	10.985 (0.0)	93.1 (4.8)	104.8
Ne IX	6.66	11.0010	11.005 (1.5)	35.6 (4.2)	22.1
Fe XXIII	7.27	11.0190	11.024 (1.0)	76.3 (7.2)	67.2
Fe XXIV	7.42	11.0290	11.036 (0.5)	72.9 (7.3)	88.3
Fe XVII	6.76	11.1310	11.138 (2.0)	18.9 (3.8)	19.8
Fe XXIV	7.42	11.1760	11.179 (0.0)	166.7 (6.7)	159.2
Fe XVII	6.76	11.2540	11.255 (1.5)	24.6 (4.9)	27.4
Fe XXIV	7.42	11.2680	11.268 (1.0)	46.9 (5.2)	36.5
Fe XVIII	6.89	11.3260	11.330 (0.5)	48.1 (4.0)	38.7
Fe XVIII	6.88	11.5270	11.531 (1.0)	48.9 (4.4)	37.8
Ne IX	6.64	11.5440	11.551 (0.5)	68.7 (4.8)	63.6
Fe XXIII	7.26	11.7360	11.744 (0.5)	238.8 (7.4)	223.9
Fe XXII	7.16	11.7700	11.775 (0.0)	209.9 (7.0)	188.6
Fe XXII	7.15	11.9320	11.937 (1.0)	65.7 (4.9)	27.2
Ne X	6.94	12.1350	12.137 (3.5)	1839.0 (19.3)	1838.2
Fe XXIII	7.25	12.1610	12.162 (1.0)	120.4 (9.2)	119.6
Fe XVII	6.75	12.2660	12.268 (1.0)	70.9 (9.7)	60.0
Fe XXI	7.09	12.2840	12.289 (0.5)	304.5 (12.2)	342.4
Fe XXII	7.15	12.7540	12.756 (0.5)	79.9 (6.6)	64.5
Fe XX	7.03	12.8240	12.831 (1.0)	140.1 (10.0)	60.1
Fe XX	7.03	12.8460	12.849 (1.0)	123.9 (14.1)	140.4
Fe XX	7.03	13.3850	13.381 (2.0)	47.1 (9.2)	33.0
Fe XIX	6.96	13.4230	13.434 (2.5)	42.2 (7.9)	24.1
Ne IX	6.61	13.4470	13.452 (0.5)	414.6 (14.3)	443.3
Fe XIX	6.96	13.4620	13.471 (1.0)	92.5 (8.7)	55.8
Fe XIX	6.96	13.5180	13.527 (0.5)	188.4 (12.1)	211.4

Table 6 — *Continued*

Ion	$\log T_{\rm max}$ log [K]	λ_0 [Å]	$\lambda_{\rm obs}$ [Å(m Å)]	f [10^{-6} phot cm^{-2} s^{-1}]	$f_{\rm model}$
(1)	(2)	(3)	(4)	(5)	(6)
Ne IX	6.58	13.5520	13.558 (1.0)	101.5 (9.2)	71.7
Fe XIX	6.96	13.6450	13.654 (1.5)	55.9 (6.9)	33.8
Ne IX	6.59	13.6990	13.703 (0.5)	279.7 (11.5)	249.3
Fe XX	7.02	13.7670	13.771 (2.5)	54.8 (7.3)	23.2
Fe XIX	6.96	13.7950	13.800 (1.0)	102.6 (8.6)	90.1
Fe XVIII	6.87	14.2080	14.209 (0.5)	309.1 (14.3)	387.5
Fe XVIII	6.87	14.2560	14.263 (1.0)	87.1 (7.1)	76.7
Fe XX	7.02	14.2670	14.276 (1.5)	54.0 (12.1)	39.3
Fe XVIII	6.87	14.3430	14.350 (1.5)	52.1 (7.9)	43.0
Fe XVIII	6.87	14.3730	14.379 (1.0)	112.8 (10.0)	92.5
Fe XVIII	6.87	14.5340	14.541 (1.0)	115.8 (12.8)	76.8
Fe XIX	6.96	14.6640	14.671 (1.0)	72.4 (9.6)	85.0
O VIII	6.71	14.8210	14.823 (1.0)	60.4 (8.5)	46.9
Fe XVII	6.73	15.0140	15.017 (0.5)	542.6 (18.0)	563.4
Fe XIX	6.95	15.0790	15.085 (1.0)	118.9 (9.5)	87.4
O VIII	6.70	15.1760	15.180 (1.0)	118.1 (9.3)	106.7
Fe XIX	6.96	15.1980	15.205 (1.5)	49.5 (7.5)	54.5
Fe XVII	6.72	15.2610	15.266 (0.5)	190.4 (10.8)	174.6
Fe XVII	6.70	15.4530	15.459 (2.0)	32.7 (6.9)	28.8
Fe XVIII	6.87	15.4940	15.493 (3.0)	20.2 (6.4)	9.4
Fe XVIII	6.86	15.6250	15.629 (1.0)	96.0 (9.2)	118.6
Fe XVIII	6.86	15.8240	15.829 (1.5)	58.2 (8.5)	71.0
Fe XVIII	6.86	15.8700	15.876 (1.0)	67.3 (8.9)	42.8
Fe XVIII	6.86	16.0710	16.079 (0.5)	244.5 (14.2)	199.9
Fe XIX	6.95	16.1100	16.112 (1.0)	75.9 (9.8)	92.6
Fe XVIII	6.87	16.1590	16.169 (2.0)	35.9 (8.0)	52.1
Fe XVII	6.70	16.7800	16.781 (0.5)	328.9 (17.7)	351.5
Fe XVII	6.71	17.0510	17.056 (0.5)	443.8 (21.3)	413.6
Fe XVII	6.70	17.0960	17.101 (0.5)	470.2 (21.8)	476.8
Fe XVIII	6.86	17.6230	17.627 (1.5)	108.1 (13.9)	121.7
O VII	6.38	17.7680	17.758 (5.5)	19.0 (9.8)	13.2
O VII	6.37	18.6270	18.633 (2.0)	74.1 (14.1)	37.3
Ca XVIII	7.07	18.6910	18.685 (5.5)	18.8 (11.5)	25.5
O VIII	6.65	18.9700	18.974 (0.0)	2142.0 (60.9)	2140.0
Ca XVIII	7.03	19.6420	19.627 (15.0)	8.1 (10.8)	18.2
Ca XVIII	7.03	19.7950	19.793 (8.5)	16.2 (13.5)	36.3
N VII	6.55	19.8260	19.830 (5.5)	35.5 (15.8)	29.6
N VII	6.53	20.9100	20.912 (3.0)	103.8 (23.7)	99.6
O VII	6.34	21.6020	21.605 (2.0)	212.8 (32.5)	247.0
O VII	6.32	21.8020	21.815 (8.5)	41.4 (22.4)	35.3
O VII	6.32	22.0980	22.101 (2.0)	211.5 (37.1)	155.1
N VII	6.49	24.7820	24.785 (1.0)	707.4 (62.0)	667.3

Note. — Lines used in the EMD and abundance reconstruction for HR 1099. Columns are analogous to those in Table 5.

APPENDIX

SUPPLEMENTAL MATERIAL

Line Flux Ratio Residuals

Figure 9 shows in detail the line flux ratio residuals (model to data) against wavelength, temperature, and line flux. Features with ratios roughly between 0.5 and 2.0 were used in the emission measure modeling. We include some of the weaker lines (such as of K, Na, and Al) which were not used, but were later fit for abundances post facto using the emission measure solution. The figures show that there are a significant number of lines spanning the wavelength and temperature ranges, and of significant quality for emission measure modeling.

A small bias can be seen in that residuals are slightly more likely to be high than low. This is more clearly seen in the histogram of the residuals in Figure 10. There is a tail above a ratio of 1.4, and it is similar in both stars. Looking at the lower panel of Figure 9 we can see that this bias is more prevalent in the weaker lines. Hence, we believe it is due to inclusion of unresolved blends in the measured flux which are not accounted for in the model flux. A systematically low continuum would also produce high residuals, but the flat residuals seen in Figures 1, 5, 6 and 7 argue against that explanation, as do other well modeled weak lines.

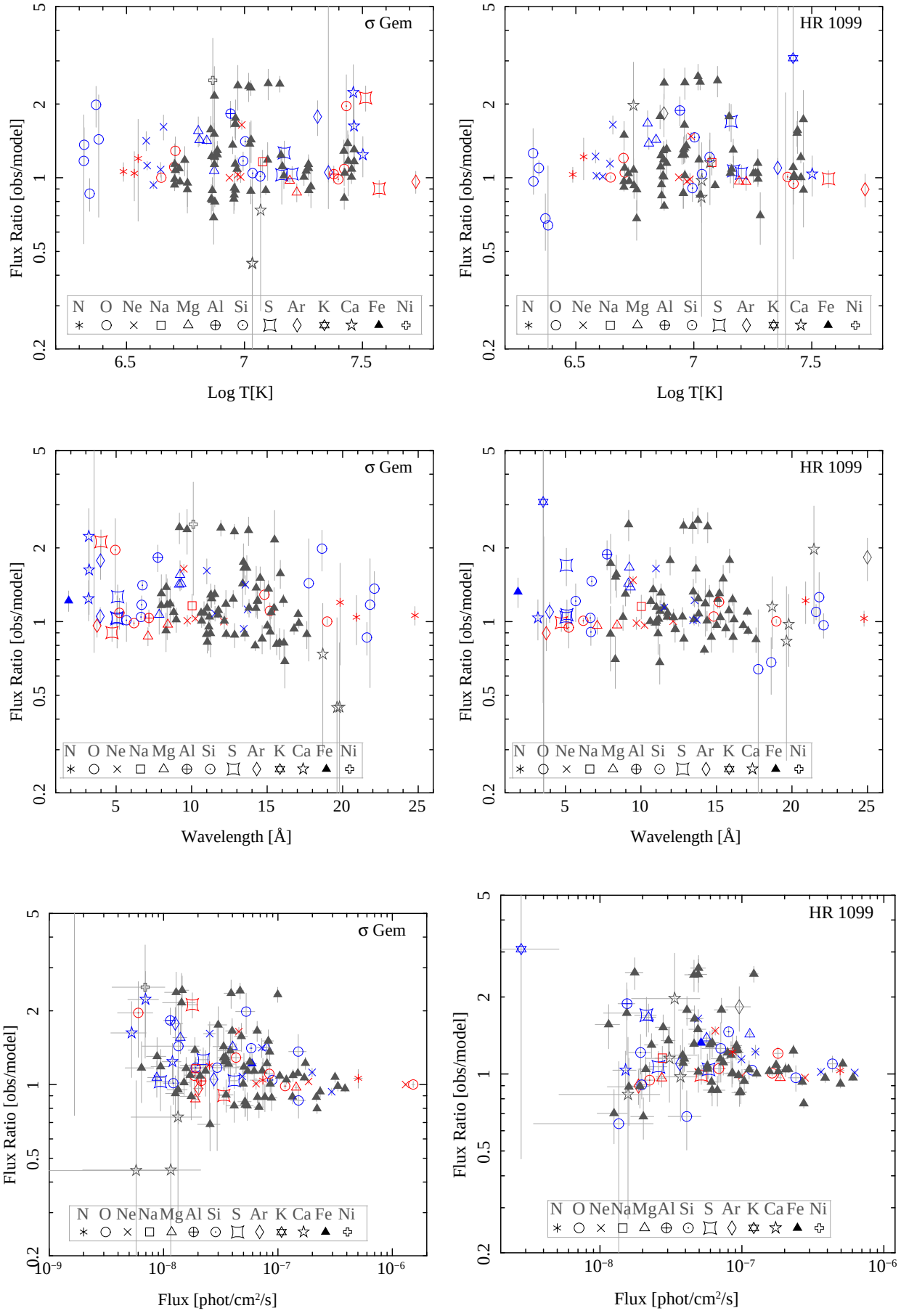

Figure 9. Line flux ratio residuals for σ Gem (left column) and HR 1099 (right column) against temperature of peak emissivity (top row), wavelength (middle row), and line flux (bottom row). Elements are plotted with different symbols. H-like lines are in red, He-like are blue, and others (primarily Fe) are gray.

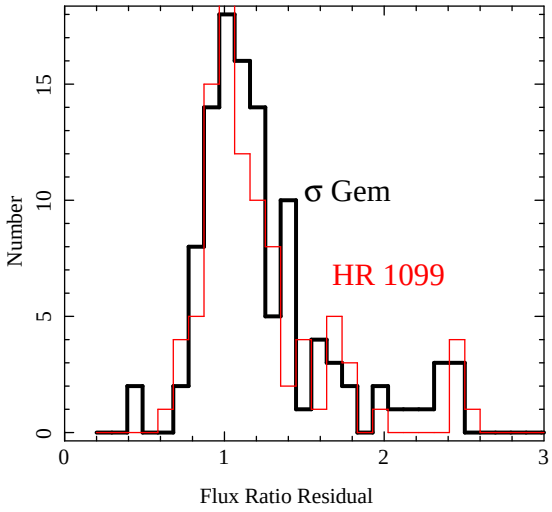

Figure 10. Histogram of the line flux ratio residuals for σ Gem (thicker or dark line) and HR 1099 (thinner or red line). There is a small systematic bias for outliers to have high residuals. This is likely due to unresolved blends in weak lines making the measured flux higher than expected.

Emission Measure Tables

The following tables give the emission measure distributions for σ Gem (Table 7), HR 1099 (Table 8), and the solar flare (Table 9).

Table 7
σ Gem Emission Measure Distribution

$\log T$ [log K] (1)	EM_{51} (2)	EM_{low} [10^{51} cm^{-3}] (3)	EM_{high} (4)
6.3	2.4	1.7	3.2
6.4	8.5	6.2	10.9
6.5	21.9	18.8	25.0
6.6	36.9	32.8	41.0
6.7	35.4	31.5	39.3
6.8	61.1	55.0	67.2
6.9	84.5	77.2	91.8
7.0	304.5	292.2	316.7
7.1	248.2	231.5	264.9
7.2	392.1	370.3	413.9
7.3	301.3	279.8	322.8
7.4	138.7	124.4	153.0
7.5	109.0	91.6	126.4
7.6	157.6	134.6	180.6
7.7	240.2	211.0	269.5
7.8	182.5	136.9	228.1
7.9	60.1	41.4	78.8
8.0	13.6	9.6	17.5
8.1	3.3	2.4	4.1
8.2	1.0	0.8	1.2
8.3	0.5	0.4	0.6

Note. — Emission measure values corresponding to the data plotted in Figure 3. Values are integrated over uniform logarithmic temperature bins of $0.1\,\mathrm{dex}$. Columns 3 and 4 give the 1σ statistical uncertainties based on line-flux uncertainties and Monte-Carlo emission measure reconstruction runs.

Table 8
HR 1099 Emission Measure Distribution

$\log T$ [log K] (1)	EM_{51} (2)	EM_{low} [10^{51} cm^{-3}] (3)	EM_{high} (4)
6.3	2.1	1.1	2.1
6.4	8.5	4.1	7.3
6.5	25.9	12.6	16.8
6.6	39.4	22.0	27.4
6.7	34.5	21.1	26.3
6.8	41.1	36.8	45.0
6.9	94.4	51.7	61.5
7.0	179.9	195.6	212.0
7.1	169.3	154.9	177.3
7.2	198.3	247.9	277.1
7.3	233.5	187.3	216.1
7.4	205.3	83.2	102.4
7.5	151.5	61.3	84.6
7.6	103.4	90.1	120.9
7.7	66.4	141.2	180.4
7.8	38.1	91.7	152.7
7.9	19.5	27.7	52.8
8.0	8.9	6.4	11.7
8.1	3.9	1.6	2.7
8.2	1.7	0.5	0.8
8.3	0.8	0.3	0.4

Note. — Emission measure values corresponding to the data plotted in Figure 3. Values are integrated over uniform logarithmic temperature bins of $0.1\,\mathrm{dex}$. Columns 3 and 4 give the 1σ statistical uncertainties based on line-flux uncertainties and Monte-Carlo emission measure reconstruction runs.

Table 9
Solar Flare Emission Measure

$\log T_{low}$ [log K] (1)	$\log T_{high}$ (2)	EM_{57} [10^{57} cm^{-3}] (3)
6.50	6.53	19170.53
6.53	6.57	8624.91
6.57	6.60	956.94
6.60	6.64	24.58
6.64	6.67	0.17
6.67	6.92	0.00
6.92	7.17	0.03
7.17	7.21	0.00
7.21	7.24	0.29
7.24	7.28	59.82
7.28	7.32	467.73
7.32	7.35	97.59
7.35	7.39	0.60
7.39	7.42	0.01

Note. — Emission measure values corresponding to the data plotted in Figure 3. Values are integrated over variable-width logarithmic temperature bins.